




**Dual-polarization topological rainbow concentrators based on glide-reflection symmetry**

Quanxin Luo <sup>1,\*</sup>, Bojian Shi,<sup>1,\*</sup> Rui Feng,<sup>1,†</sup> Donghua Tang,<sup>2</sup> Tongtong Zhu,<sup>3</sup> Yongyin Cao <sup>1</sup>,  
Fangkui Sun,<sup>1,‡</sup> and Weiqiang Ding <sup>1,4,§</sup>

<sup>1</sup>*Institute of Advanced Photonics, School of Physics, Harbin Institute of Technology, Harbin 150001, China*

<sup>2</sup>*Department of Physics, School of Science, Northeast Forestry University, Harbin 150040, China*

<sup>3</sup>*School of Physics, Dalian University of Technology, Dalian 116024, China*

<sup>4</sup>*Collaborative Innovation Center of Extreme Optics, Shanxi University, Taiyuan 030006, China*



(Received 20 January 2024; revised 27 April 2024; accepted 3 June 2024; published 8 July 2024)

Topological rainbow concentrators (TRCs) have attracted intense attention due to their capability of capturing photons with varying frequencies to distinct positions. However, the design of TRCs is not straightforward, especially for wideband and dual-polarization ones. In this paper, we propose a general and efficient methodology to realize TRCs by employing the glide-reflection symmetry operation. Starting from an ordinary photonic crystal with complete band gaps, and employing the two degrees of freedom of glide-reflection symmetry, i.e., the position of mirror reflection and the gliding length, wideband and dual-polarization TRCs are constructed successfully. Very interestingly, by monitoring the distance between the trapping positions of the two polarizations, the incident light frequency can be derived precisely. This paper introduces an efficient and flexible approach to configure TRCs, and may contribute to the wide applications in spectral analysis and polarization demultiplexing.

DOI: [10.1103/PhysRevA.110.013503](https://doi.org/10.1103/PhysRevA.110.013503)

## I. INTRODUCTION

Topological rainbow concentrators (TRCs) exhibit the capacity of dispersing and trapping different frequency components to distinct spatial locations, while possessing the merit of topological robustness to defects [1,2]. Due to these merits, they hold broad prospects for applications in multiple fields, such as optical information processing [3] and optical storage [4]. Typically, TRCs can be achieved through the combination of slow-light effect and topological properties. Slow-light effect results in frequency-dependent deceleration of electromagnetic waves within a specific frequency range, which causes light to be trapped to different locations [5–9]. However, due to the enhanced interaction between light and matter [10], slow-light systems are highly sensitive to defects, leading to significant backward scattering and loss. In order to overcome this challenge, the robustness of topological photonics offers an efficient solution.

Currently, there are two approaches to implement the topological properties in rainbow devices. The first uses photonic crystals (PCs) that possess topological properties inherently [11–13], such as those achieved through photonic quantum spin Hall effect [14,15] or photonic quantum valley Hall effect [16]. However, due to the presence of topological phase transition and band degeneracy [17,18], the bandwidths of these structures tend to be narrow. The other approach en-

tails the construction of synthetic dimension [1,2]. However, the valid implementation techniques are relatively limited up to now. Moreover, current TRCs are predominantly realized for transverse electric (TE) waves or transverse magnetic (TM) waves only, but not for both polarizations. Actually, polarization dependent optical manipulation holds numerous applications in diverse domains, such as in biosensing [19,20] and polarization division multiplexing to enhance communication capacity [21–24]. Therefore, it is highly desirable to explore TRCs valid for both TE and TM polarizations simultaneously with enhanced bandwidth and reliability.

Recently, glide-reflection symmetry is found to be useful in acoustics for the generation of topological properties by tuning the glide length [25]. In this paper, we extend the glide-reflection symmetry operation to optics. More importantly, we complete the glide-reflection operation by introducing the new degree of freedom, i.e., the position of mirror symmetry. Then, two wideband and dual-polarization TRCs are constructed by using inclined axis and synthetic-dimension methods, respectively. This paper contributes an efficient and general approach to configuring TRCs, and will broaden the application of topological rainbow devices in diverse domains, such as spectral analysis and polarization separation.

## II. RESULT AND DISCUSSION

### A. Topological properties of glide-reflection symmetry

Glide-reflection symmetry is the combination of mirror reflection and translation operations. A previous paper only discussed the effects of the glide parameter [25]. In fact, glide-reflection symmetry has two degrees of freedom, which

\*These authors contributed equally to this work.

†Contact author: fengrui\_0223@163.com

‡Contact author: fksun@hit.edu.cn

§Contact author: wqding@hit.edu.cn

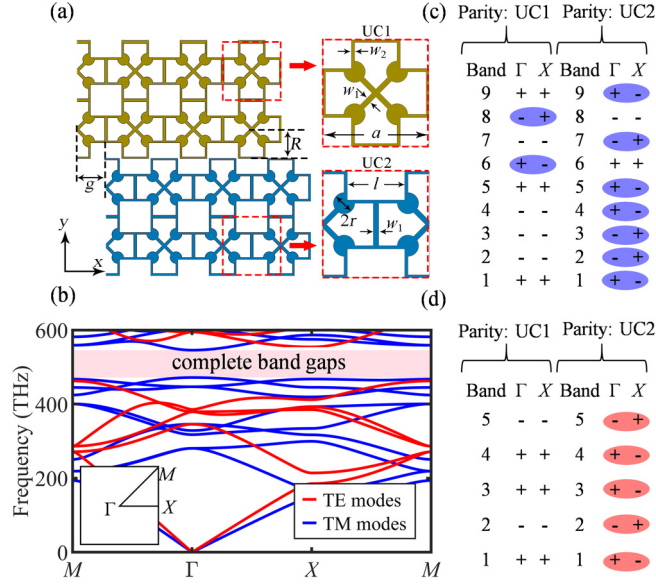


FIG. 1. Schematic and properties of the structure. (a) Schematic of the PC with glide-reflection symmetry, where  $a = 500$  nm,  $g = 0.5a$ ,  $R = 0.5a$ ,  $r = 0.1a$ ,  $w_1 = 0.05a$ ,  $w_2 = 0.03a$ ,  $l = 0.6a$ .  $R$  denotes the position of the mirror reflection, defined as the distance from the interface to the center of the nearest unit cell.  $g$  represents glide length, defined as the displacement in the  $x$  direction of the lower PC relative to the upper PC.  $a$  is the lattice constant. The relative permittivity of the medium is 11.7. The remaining portions are air, with a relative permittivity set to 1. (b) The complete band gap of the PC exists above the ninth TM band and the fifth TE band, with a relative bandwidth of 14.5%. (c, d) Parity of the TM and TE modes at the  $\Gamma$  and  $X$  points, respectively, where the eigenmodes with opposite parity are marked by blue and red ellipses.

are the position of the mirror reflection ( $R$ ) and the glide length ( $g$ ). The structure and related parameters of a PC with glide-reflection symmetry are shown in Fig. 1(a). The interface between the upper and lower PCs corresponds to the axis of mirror reflection symmetry.  $R$  is defined as the distance from the interface to the center of the nearest unit cell, and  $g$  is defined as the displacement in the  $x$  direction of the lower PC relative to the upper PC. UC1 and UC2 represent the unit cells of the upper and lower PCs, respectively. Actually, the unit cells are obtained by superposing a unit cell with a connected dielectric wall, and another unit cell with an isolated dielectric atom, which tends to generate band gaps for TE and TM polarizations, respectively. Therefore, the superposition of them results in a complete band gap (CBG) for both polarizations. More details about the unit-cell design can be found in Appendix A.

In Fig. 1(a), UC2 is obtained from UC1 by applying the glide-reflection symmetry operation with the mirror reflection position of  $R = 0.5a$  and the glide length of  $g = a/2$  along the  $x$  direction. It is evident that both unit-cell structures possess the same band structure. As shown in Fig. 1(b), it possesses complete TE and TM band gaps with a large relative bandwidth of 14.5%. The band gap exists above the ninth TM band and the fifth TE band. By virtue of the inversion symmetry of the unit cell within the structure, the topological properties of UC1 and UC2 in the  $x$  direction can be determined gauge

independently by the parities at the  $\Gamma$  and  $X$  points, which are defined as [26–28]

$$\theta_x = \pi \left( \sum_n q_x^n \bmod 2 \right), \quad (-1)^{q_x^n} = \frac{\eta(X)}{\eta(\Gamma)}, \quad (1)$$

where  $\eta$  denotes the parity ( $\pm 1$ ),  $\theta_x$  is the Zak phase in the  $x$  direction, and the summation is over all the occupied bands.

We calculated the eigenmode patterns numerically of each band at  $\Gamma$  and  $X$  for both TE and TM modes, and extracted their parities by checking their symmetry under inversion operations. If an eigenmode pattern coincides with itself after a  $180^\circ$  rotation around the geometric center, it is classified as even parity (+), otherwise it is classified as odd parity (-). The parities of related modes are shown in Figs. 1(c) and 1(d). According to Eq. (1), it can be deduced that the Zak phases of both TE and TM modes in UC1 are zero, indicating topological triviality. Conversely, for UC2, the Zak phases of TE and TM modes are  $\pi$ , signifying topological nontriviality. This demonstrates the topological protection of both TE and TM modes in the glide-reflection symmetry structure. Furthermore, besides Zak phases, the topological properties of the system can also be described using the Wannier center position and symmetry indicators [29,30]. These results set solid foundations for the glide-reflection symmetry based TRCs, as detailed below.

### B. Topological rainbow constructed via an inclined mirror reflection symmetry axis

In this section, we discuss TRCs via an inclined mirror reflection axis, as illustrated in Fig. 2(a), which is achieved through gradual variation of  $R$  from  $0.4a$  to  $0.5a$ . The variation of  $R$  causes the change of PC in the  $y$  direction. However, as  $x$  and  $y$  directions are orthogonal, this change has no impact on the Zak phase in the  $x$  direction, and hence the two-dimensional Zak phase. Therefore, the topological properties remain unaffected by changing  $R$ . The band structures of TE and TM interface states are separately illustrated in Figs. 2(c) and 2(d). Based on the observation of the dispersion bands, it is evident that they display degeneracy at the  $X$  point (i.e.,  $k_x = \pi/a$ ), which is determined by the combined effect of time-reversal symmetry and glide-reflection symmetry at  $g = a/2$  [25,31,32]. Furthermore, it is evident that two surface state dispersive bands are present within each gap of the glide-reflection structures. Additionally, a degeneracy point for TE modes is observed at the interior of the Brillouin zone. These phenomena are further elucidated in Appendix C. Additionally, as  $R$  increases, the dispersion bands of both TE and TM interface states shift downwards, but can separate from each other clearly.

By calculating the slope  $\partial\omega/\partial k_x$  of the dispersion bands, the group velocity  $v_g$  is obtained, as shown in Figs. 2(e) and 2(f). When  $v_g$  approaches zero, it corresponds to a flat band, where light of a specific frequency will be localized within the corresponding structure, and form a trapped state. On the other hand, when  $v_g$  is not equal to zero, light will propagate along the interface as a transport state. The underlying physical mechanism is a Bragg scattering, which can be categorized into three main types [33]. The first type

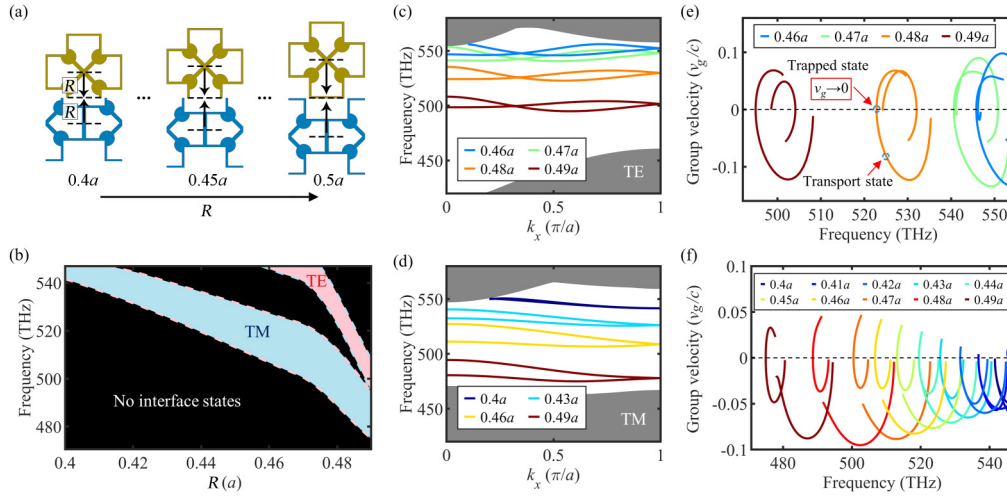


FIG. 2. Effects of mirror reflection position  $R$  on the optical properties of the interface states. (a) Schematic of the PC with glide-reflection symmetry for different  $R$ 's from  $0.4a$  to  $0.49a$ . (b) Frequency ranges of TE and TM interface states change with  $R$ . (c), (d) Dispersion bands of TE and TM interface states, respectively. The legends and colors show different  $R$ . (e), (f) Group velocity diagrams of TE and TM interface states, respectively.

occurs at the center of the Brillouin zone, denoted as the  $\Gamma$  point. The second type is observed at the boundary of the Brillouin zone, marked as the  $X$  point. The third type arises from the anticrossing induced by mode coupling at the interior of the Brillouin zone. All three cases are manifested within the structures discussed in this paper. By utilizing the trapped states, the glide-reflection interface can spatially trap light of different frequencies at different  $R$  locations, resulting in the rainbow trapping. Figure 2(b) illustrates the frequency range of TE and TM interface states as  $R$  changes. It can be observed that the frequency ranges of TE and TM interface states for the same structure are distinct and separated. In other words, light with the same frequency but different polarization will be trapped in different structures. Therefore, by constructing structures with continuously changing reflection positions  $R$ , the separation of TE and TM light can be achieved.

Inspired by the analysis mentioned above, we introduce an inclined mirror reflection symmetry axis to the structure, as depicted in Fig. 3(a), where the  $x$  axis is inclined at a small angle  $\theta$  to obtain the  $x'$  axis. The number of unit cells along the  $x$  direction is denoted as  $nx$ . In the schematic diagram of Fig. 3(a),  $nx = 2.5$  is shown for clarity. The upper portion of the crystal is then reflected as a whole along the  $x'$  axis and glides along the  $x'$  axis. The glide length along the  $x$  axis is set to be  $0.5a$ , forming a glide-reflection symmetry interface with gradient  $R$ . In numerical simulation,  $nx$  is selected to be  $nx = 60$  while maintaining the gradient change of  $R$  from  $0.4a$  to  $0.49a$ . The structure is excited by a plane wave along the  $y$  direction. An incident plane wave is introduced from the upper boundary, while the remaining boundaries are treated as scattering boundary conditions. The simulation is established in a Cartesian coordinate system. For the TE mode, electromagnetic waves are defined by the magnetic field, with the relative intensity of the magnetic field set as  $(0, 0, 1)$ . For the TM mode, electromagnetic waves are defined by the electric field, with the relative intensity of the electric field set as  $(0, 0, 1)$ .

The simulated results are illustrated in Fig. 3(e), which clearly demonstrate that light of various frequencies is localized at distinct positions when incident from the top. Additionally, the localized positions for TE and TM modes differ also, corroborating the previously discussed predictions of polarization separation. As shown in Fig. 3(b), the normalized intensity distributions of TE and TM modes of light at different frequencies along the  $x'$  axis are plotted. The positions of peak intensities are denoted by black circles. Furthermore, Fig. 3(c) illustrates the frequency-dependent changes in the peak positions for TE and TM modes. It becomes evident that the localized positions for both polarizations approximately linearly change with the frequency. The distance between them also varies with frequency, providing further support to the observations in Fig. 2(b). Figure 3(d) intuitively illustrates the linear relations between these variations.

### C. Topological rainbow based on synthetic dimension

In this section, we investigate the influence of the glide length  $g$  to the synthetic dimension based TRC. Inspired by Lu *et al.* [2], we introduce the concept of synthetic dimension, including the glide length  $g$  and the Bloch wave vector  $(k_x, k_y)$ . Then a three-dimensional parametric space  $(k_x, k_y, g)$  is formed, where all three parameters exhibit periodicity. The Zak phase of the system varies with the glide length  $g$ . When  $g$  changes by one lattice constant, it exhibits topological properties, and can be described by the Chern number. Keeping  $k_y$  fixed, for each  $g$ , the Zak phase of the  $n$ th band is defined as [34]

$$\theta_n(k_y, g) = \int_{-\pi/a}^{\pi/a} \langle u_n(k_x, k_y, g) | i \frac{\partial}{\partial k_x} | u_n(k_x, k_y, g) \rangle dk_x \quad (2)$$

where  $|u_n(k_x, k_y, g)\rangle$  represents the periodic component of the Bloch function.

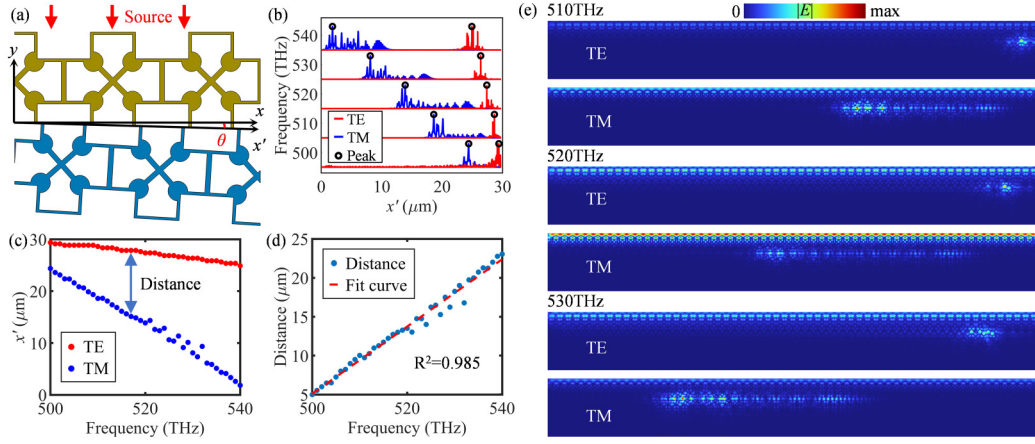


FIG. 3. TRC constructed via inclined mirror reflection symmetry axis. (a) The schematic diagram of the structure. By inclining the  $x$  axis at a small angle  $\theta$ , the  $x'$  axis is obtained. Then, reflecting and translating the upper portion of the PC along the  $x'$  axis, the reflection position  $R$  continuously changes within the range of  $0.4a$  to  $0.49a$ . The structure is excited by plane wave along the  $y$  direction. (b) Normalized intensity distribution of TE and TM modes at different frequencies along the  $x'$  axis. (c) The variation of peak intensity positions for TE and TM modes with frequency. (d) The variation of separation distances between TE and TM modes with frequency, with a red dashed line representing the fit curve. (e) Electric intensity distributions of TE and TM modes at frequencies of 510, 520, and 530 THz, respectively. The simulation employs  $nx = 60$  unit cells along the  $x$  direction.

By applying the Bloch theorem, we can deduce the following result:

$$\theta_n(k_y, g) = \theta_n(k_y, 0) + \frac{2\pi g}{a} \pmod{2\pi}. \quad (3)$$

Please refer to Appendix B for the detailed deriving process of Eq. (3). According to Eq. (3), it is evident that the Zak phase of each band varies linearly with  $g$ . For bands with an initial Zak phase of zero, the variation is illustrated in Fig. 4(a). Due to the periodic nature of both the Zak phase and  $g$ , they can be visualized as a torus, and the winding number of the Zak phase corresponds to the Chern number [35]. When  $g$  continuously varies from  $-a/2$  to  $a/2$ , the change in the Zak phase divided

by  $2\pi$  yields the Chern number:

$$C_n = \frac{1}{2\pi} \int_{-a/2}^{a/2} d\theta_n(k_y, g). \quad (4)$$

The dispersion bands of the interface states for TE and TM modes under different glide lengths  $g$  are presented in Figs. 4(c) and 4(d), respectively. Subsequently, the group velocities of the interface states for each structure are calculated, as depicted in Figs. 4(e) and 4(f). When the group velocity approaches zero, it signifies that the structure will trap light of corresponding frequency for TE or TM modes, respectively. Figure 4(b) illustrates the variation of frequency ranges of TE and TM polarizations with the changing of  $g$ . It can be observed that, similar to Fig. 2(b), TE and TM modes can

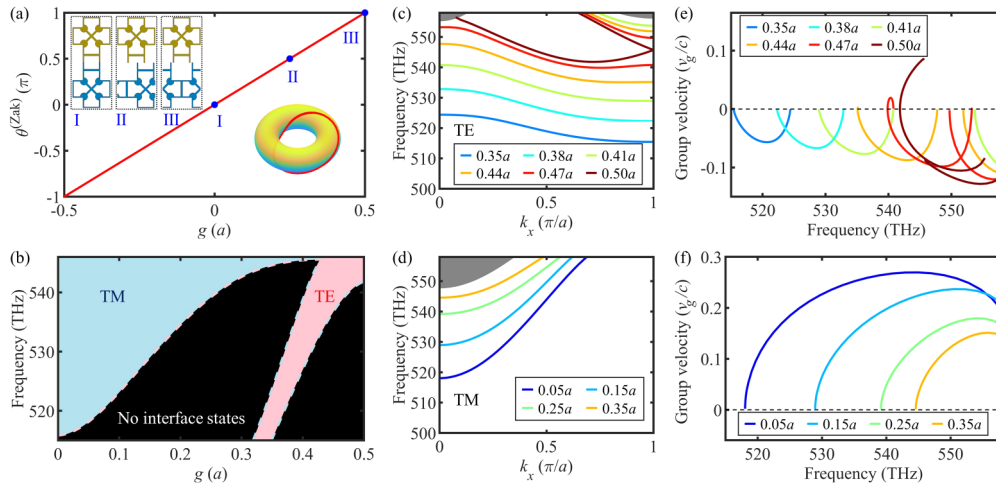


FIG. 4. Effects of glide length  $g$  on the optical properties of the interface states. (a) Evolution of Zak phases with parameter  $g$ . The inset presents the diverse geometric structures associated with different  $g$ . The torus structure is formed through the fusion of equivalent edges. (b) The frequency range of TE and TM interface states varies with the glide length. (c), (d) Dispersion bands of the TE and TM interface states are shown respectively, with different colored curves representing different structures. (e), (f) Group velocity diagrams of TE and TM interface states, respectively.



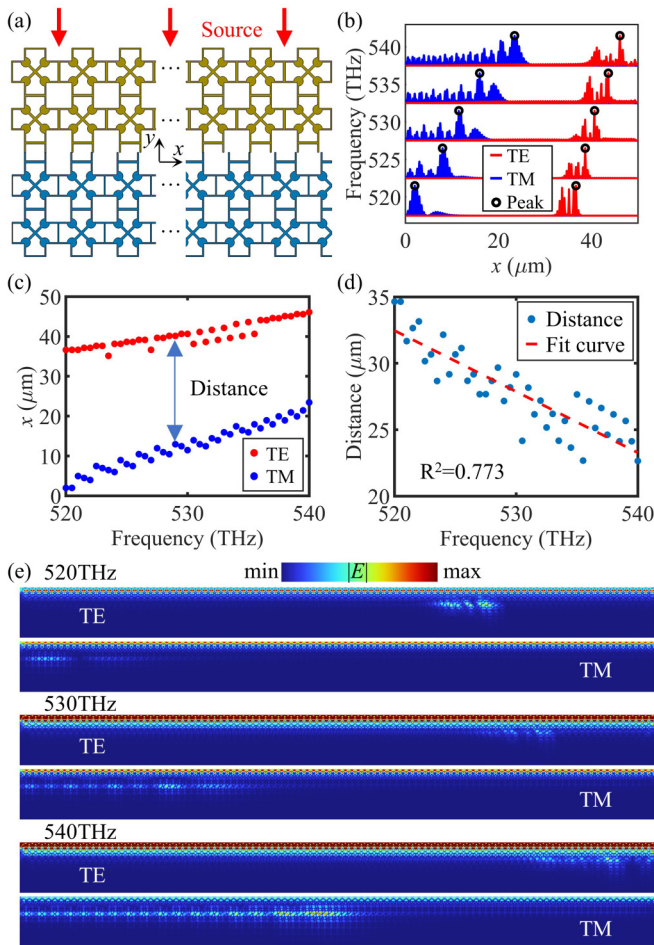


FIG. 5. TRC based on synthetic dimension of  $g$ . (a) The schematic diagram of the synthetic dimension TRC, characterized by the continuous change of the glide length  $g$ . (b) The normalized intensity distributions of TE and TM modes on the interface. (c) The frequency-dependent variation of peak intensity positions for TE and TM modes. (d) The separation distances between TE and TM modes exhibit frequency-dependent changes, with a red dashed line representing the fit curve. (e) The electric intensity distributions of TE and TM modes at frequencies of 520, 530, and 540 THz, respectively.

separate from each other within a certain frequency range. Light of the same frequency will be trapped by structures with different glide lengths for different polarizations.

A synthetic dimension based TRC with continuously varying glide lengths  $g$  is shown in Fig. 5(a), which is excited by plane waves from the top. To facilitate the analysis, only the section from  $g = 0$  to  $0.5a$  is illustrated, as  $g = -0.5a$  to  $0.5a$  exhibits symmetry. The electric-field intensity distributions of TE and TM modes at different frequencies are shown in Fig. 5(e). From these results, it can be evident that the TE and TM modes are separated, and their separations vary with frequency as predicted. The normalized intensity distributions of TE and TM modes are shown in Fig. 5(b), with the peak positions marked by black circles. Figure 5(c) shows the variation of peak positions with frequency. It can be observed that the peak positions of TE and TM modes approximately exhibit a linear relationship with frequency. Nevertheless, the

distances between the peaks of the two polarizations display scattered variations with frequencies, as shown in Fig. 5(d). The reasons for the variances will be discussed and optimized in the following section.

#### D. Optimization of topological rainbows

As shown above, both types of TRCs can trap different light to distinct positions for TE and TM modes. However, it should be noted that the separation of intensity peaks for TE and TM modes is not entirely linear with respect to frequency. To enhance the application of these devices, it is imperative to engage in a thorough discussion of this phenomenon. Generally speaking, there are two main factors affect the linearity relation between them.

The first factor is the discrete nature of  $g$  and  $R$ . Taking the structure of the inclined axis as an example, when  $nx$  is small, the change of  $R$  is highly discrete, which consequently causes a significant variation in the dispersion band of the interface states across different unit cells. For some frequencies, it is possible to lack the corresponding units to trap them exactly (exact zero group velocity). As a result, they are compelled to reside in the regions with relatively lower group velocities. This is the main reason giving rise to the observed phenomenon of “steplike” trapping, as depicted in Fig. 3(c).

The second factor is that light of some frequencies can be trapped at multiple positions. From Fig. 2(f), it can be seen that the group velocity of TM interface states may approach zero at three distinct frequencies. This indicates that a specific frequency will be localized on three positions with different  $R$ , leading to the normalized intensity of light reaching extreme values at all three positions. Given the discrete nature of our structure, the maximum intensity may alternate between multiple positions. This phenomenon is evident in both Figs. 3(c) and 5(c).

To mitigate the effects of these two factors, the first step would be increasing the unit-cell number  $nx$  in the  $x$  direction to achieve a more continuous variation of structure. Figure 6(a) depicts the variation of the peak position of the TM mode with frequency for different  $nx$  of 15, 30, 120, and 240. It is evident that as  $nx$  increases, the steplike phenomenon significantly diminishes, resulting in a much better linear relation.

Additionally, the impact of multiple localizations can be weakened by modifying the criteria used to determine the localized positions more precisely. For this purpose, we select a critical value  $\delta$ , and extract all positions where the normalized electric intensity exceeds  $\delta$ . Subsequently, we calculate the median value to determine the localized position. In Fig. 6(b), the change in the localized positions of the TE mode with frequency is depicted for various  $\delta$  of 0.5, 0.7, 0.9, and 1.0. As  $\delta$  decreases gradually within a certain range, the phenomenon of multiple localizations weakens, leading to a notable increase in the linearity of the localized positions with respect to frequency.

Based on the aforementioned approaches, optimizations are carried out for both the inclined axis TRC and the synthetic dimension TRC. Figures 6(c) and 6(d) present the frequency-dependent variations in the interval between localized positions for the TE and TM modes in both the inclined

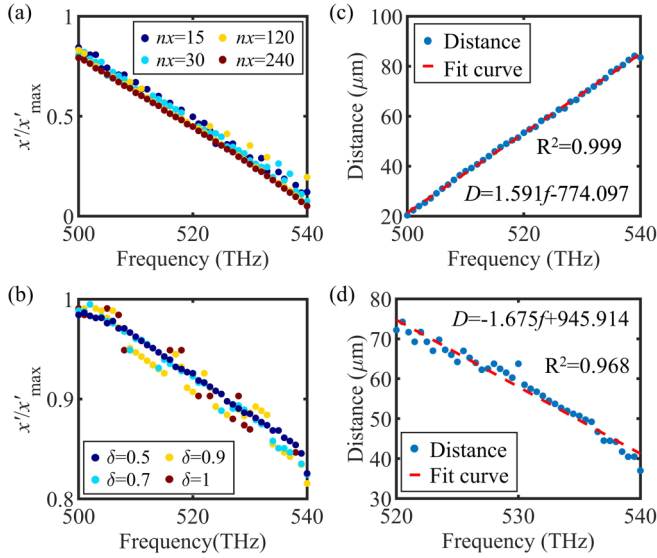


FIG. 6. Optimization of TRCs. (a) Variation of the peak positions of TM mode in the inclined axis TRC with frequency, where  $nx$  represents the quantity of unit cells in the  $x$  direction. Clearly, with the increase of  $nx$ , the deviations decrease obviously. (b) Changes of the localized positions of TE mode in the inclined axis TRC with frequency, where  $\delta$  serves as the threshold for determining the localized positions. (c) The interval between localized positions of TE and TM modes in the inclined axis TRC.  $nx = 240$  and  $\delta = 0.5$ . (d) The interval between localized positions for the TE and TM modes in the synthetic dimension TRC.  $nx = 240$  and  $\delta = 0.8$ .

axis TRC ( $nx = 240$ ,  $\delta = 0.5$ ) and the synthetic dimension TRC ( $nx = 240$ ,  $\delta = 0.8$ ). Fitted curves, along with their equations, are provided in the figures also, demonstrating a high level of linearity.

In addition, the TE mode performs much better than the TM mode in spatial localization in Fig. 3. This is due to the existence of numerous structures supporting their propagation, as evident from Fig. 2(b). For instance, at 520 THz, the range of reflection positions  $R$  corresponding to TM interface modes spans from  $0.440a$  to  $0.474a$ , whereas for TE modes, the range of reflection positions  $R$  is less than  $0.004a$ . This corresponds to the more localized nature of TE modes. Indeed, designing unit-cell structures via algorithms can narrow the range of structural variations for TE and TM modes at the same frequency, which requires further investigation.

### III. CONCLUSION

This paper presented a general and efficient approach to configuring TRCs based on glide-reflection symmetry. By utilizing the two degrees of freedom of the glide-reflection symmetry, i.e., the position of the mirror reflection ( $R$ ) and the glide length ( $g$ ), two kinds of dual-polarization TRCs are constructed from an ordinary photonic crystal unit cell with complete band gap. The first kind introduces an inclined axis, which is protected by the topological properties of glide-reflection symmetry. The second kind is based on synthetic dimensions by continuously varying the glide length  $g$ . Both the devices can trap light at separate positions for different frequencies and different polarizations. Interestingly, the two

devices not only enable the separation of TE and TM modes, but also can determine the frequency of incident light by utilizing the interval distances between the trapping positions. This dual determination of frequency achieves the purpose of spectral and polarization analysis.

These devices reported in this paper have potential applications in various areas such as frequency division multiplexing, and spectral imaging. Due to the principle of the device relying on the variations of two inherent degrees of freedom of the glide-reflection symmetry, as well as the presence of a complete band gap, its operation frequency center and operation bandwidth can be shifted and optimized by tuning the crystal unit cell. Moreover, this method of implementing TRCs is universal and readily extendable to diverse fields such as acoustics and mechanics. The introduction of inclined axis and synthetic-dimension methods based on glide-reflection symmetry provides a different approach to configuring topological rainbows, offering a platform for the implementation of topological photonic devices.

### ACKNOWLEDGMENTS

The authors acknowledge funding provided by the National Natural Science Foundation of China (Grant No. 12274105), Heilongjiang Natural Science Funds for Distinguished Young Scholars (Grant No. JQ2022A001), Fundamental Research Funds for the Central Universities (Grant No. HIT.OCEF.2021020), and the joint guidance project of the Natural Science Foundation of Heilongjiang Province (Grant No. LH2023A006).

### APPENDIX A: DESIGN OF THE UNIT CELL WITH COMPLETE BAND GAP

In the main text, we adopt a unit cell with complete band gap to construct the rainbow concentrator. Here, we show how the unit cell is determined using a universal methodology.

Normally, TE and TM band gaps do not coexist simultaneously in PCs. The presence of the TE band gap is associated with Bragg scattering, while the TM band gap primarily originates from Mie resonances [36]. When interconnected in regions of high dielectric constant, Bragg scattering makes the occurrence of TE band gaps more likely. In the PC depicted in Fig. 7(a), dielectric walls are mutually connected. As discerned from the band structure in Fig. 7(b), it is evident that the TE mode exhibits a wider band gap. When separated in regions of high dielectric constant, the optical field tends to exhibit strong localization. In this scenario, Mie resonances take precedence, leading to the emergence of TM band gaps. As depicted in Figs. 7(c) and 7(d), the PC is composed of isolated dielectric atoms, which results in a broader TM band gap.

By superposing both the unit cells together, it is possible to find a compromise that enables simultaneous band gaps for both polarizations, which is known as CBG, as illustrated in Figs. 7(e) and 7(f). The PC with a CBG was achieved through the superposition of dielectric rods interconnected by dielectric walls, followed by parametric scanning and optimization adjustments. The relative bandwidth is measured to be 14.5%, positioned above the ninth TM band and the fifth TE band.

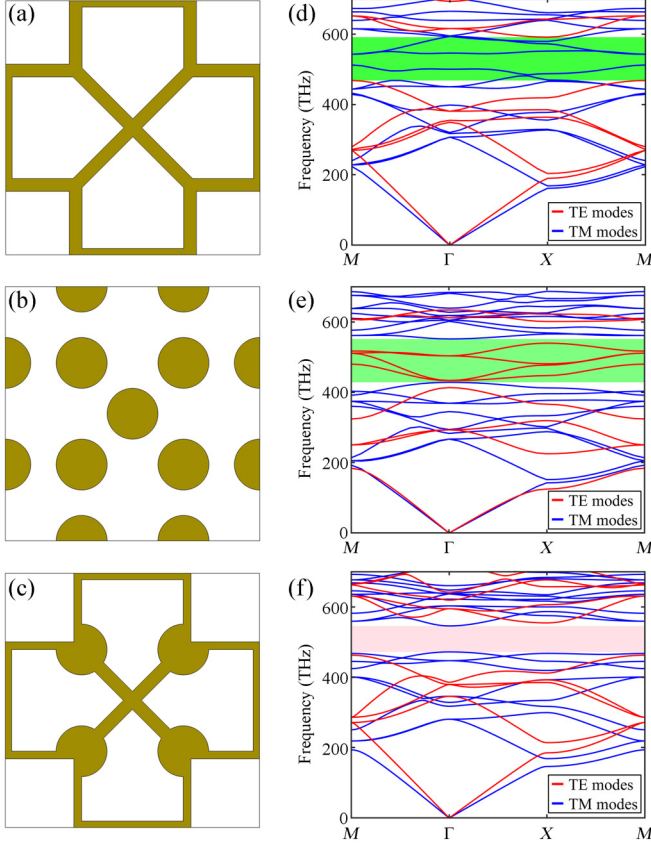


FIG. 7. Design of the unit cell with complete band gap by superposing two unit cells with TE and TM band gaps, respectively. (a) Schematic diagram of a unit cell with interconnected dielectric walls. (b) Corresponding TE band gap of the unit cell shown in (a). (c) Schematic diagram of a unit cell with isolated dielectric rods. (d) Corresponding TM band gap of the unit cell shown in (c). (e) Schematic diagram of the combination of dielectric rods connected by dielectric walls. (f) A large complete band gap is obtained for the unit cell shown in (e).

### APPENDIX B: VARIATION OF ZAK PHASE WITH $g$

Suppose photonic crystal B is obtained as a result of applying a glide translation in the  $x$  direction with  $g$  to photonic crystal A. Let the reciprocal lattice vectors be  $\mathbf{G}_1$  and  $\mathbf{G}_2$ , respectively. For the  $n$ th energy band, according to the Bloch theorem, the wave functions of crystals A and B can be written as follows:

$$\varphi_{n,\mathbf{k}}(\mathbf{r}) = e^{i\mathbf{k}\cdot\mathbf{r}} u_{n,\mathbf{k}}(\mathbf{r}) = e^{i(k_x r_x + k_y r_y)} u_{n,\mathbf{k}}(\mathbf{r}), \quad (\text{B1})$$

$$\varphi_{n,\mathbf{k},g}(\mathbf{r}) = e^{i\chi(\mathbf{k},g)} \varphi_{n,\mathbf{k}}(\mathbf{r} - g\mathbf{x}). \quad (\text{B2})$$

Since the crystal returns to its original state after a glide length of  $g = a$ , let  $\chi(\mathbf{k}, g)$  be an arbitrary periodic real function, satisfying

$$e^{i\chi(\mathbf{k}+\mathbf{G},g)} = e^{i\chi(\mathbf{k},g+a)} = e^{i\chi(\mathbf{k},g)}. \quad (\text{B3})$$

Then we have

$$u_{n,\mathbf{k},g}(\mathbf{r}) = e^{i\chi(\mathbf{k},g)} e^{-ik_x g} u_{n,\mathbf{k}}(\mathbf{r} - g\mathbf{x}). \quad (\text{B4})$$

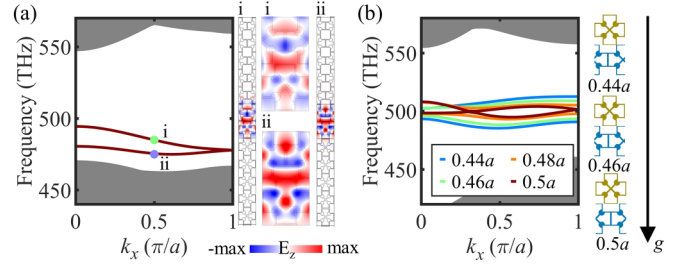


FIG. 8. (a) The band structure of TM polarization when  $R = 0.49a$  and  $g = 0.5a$  is shown. Points i and ii denote two interface modes at  $k_x = 0.5\pi/a$ , with frequencies 485.0 and 475.5 THz, respectively. The corresponding mode profiles at points i and ii are also depicted. (b) When the position of the mirror reflection is fixed at  $R = 0.49a$ , variations in the glide length  $g$  lead to the band crossing and band anticrossing phenomena in the TE mode.

Defined by the Zak phase,

$$\theta_n(B) = \int_{-\pi/a}^{\pi/a} dk_x \iint_{BZ} u_{n,\mathbf{k},g}(\mathbf{r}) i \frac{\partial}{\partial k_x} u_{n,\mathbf{k},g}(\mathbf{r}) d^2\mathbf{r}. \quad (\text{B5})$$

Substituting into Eq. (B4), we obtain

$$\theta_n(B) = \theta_n(A) + \frac{2\pi g}{a} - \left[ \chi\left(\frac{1}{2}\mathbf{G}_1 + k_y \mathbf{G}_2, g\right) - \chi\left(-\frac{1}{2}\mathbf{G}_1 + k_y \mathbf{G}_2, g\right) \right]. \quad (\text{B6})$$

Therefore, the influence of  $g$  on the Zak phase is

$$\theta_n(k_y, g) = \theta_n(k_y, 0) + \frac{2\pi g}{a} \pmod{2\pi}. \quad (\text{B7})$$

### APPENDIX C: THE EMERGENCE OF PAIRED INTERFACE STATES AND DEGENERACY POINTS

To elucidate the appearance of two surface modes within the band gap, we illustrate in Fig. 8(a) the mode profiles of interface states, using the example of TM modes. The exponential decay of electric-field intensity along the  $y$  direction indicates that both states are interface states.

Moreover, the field distribution of a photonic crystal is defined as  $\mathbf{F}(x, y, z)$ . The operator representing the glide-reflection operation is denoted as  $\hat{g}$ . The field distribution corresponds to the eigenfunctions of the operator  $\hat{g}$  with eigenvalue  $g$ :

$$\hat{g}\mathbf{F}(x, y, z) = g\mathbf{F}(x, y, z). \quad (\text{C1})$$

Applying the operator  $\hat{g}$  twice and utilizing the Bloch theorem, we obtain

$$\hat{g}\hat{g}\mathbf{F}(x, y, z) = \mathbf{F}(x + a, y, z) = e^{ik_x a} \mathbf{F}(x, y, z). \quad (\text{C2})$$

The eigenvalues of the operator  $\hat{g}$  are given by

$$g = \pm e^{ik_x a/2}. \quad (\text{C3})$$

Clearly, the field distribution can be categorized into two distinct modes. When  $g = +e^{ik_x a/2}$ , it corresponds to the “+” mode; conversely, when  $g = -e^{ik_x a/2}$ , it represents the “-” mode. From Fig. 8(a), it is evident that neither mode is purely



odd or even, but rather can be understood as linear combinations of odd and even modes, exhibiting a zigzag pattern at the interface.

Furthermore, due to the presence of time-reversal symmetry, the eigenfunctions remain unchanged under the transformation  $k \rightarrow -k$ , implying  $g = \pm e^{\pm ik_x a/2}$ . At point  $X$ ,  $k_x = \pi/a$ . For the “+” mode, we have  $g = e^{\pm i\pi/a \cdot a/2} = \pm i$ . For the “-” mode,  $g = -e^{\pm i\pi/a \cdot a/2} = \mp i$ . Both represent equivalent  $\hat{g}$ . This leads to the appearance of degenerate points at the Brillouin-zone boundary.

Another intriguing phenomenon is the existence of another degeneracy point for the TE mode in the middle of the Brillouin zone, as shown in Fig. 2(c). We attempt to explain this degeneracy point using the coupled-mode theory. The coupling coefficient  $\kappa$  between two guided modes  $n_1$  and  $n_2$  in the band gap with the same wave vector  $k$  can be defined as the overlap integral:

$$\kappa \propto \int \vec{E}_{n_1}^k(\vec{r}) \cdot \vec{E}_{n_2}^{k*}(\vec{r}) [\epsilon(x, y, z)] d^3\vec{r}. \quad (\text{C4})$$

When guided modes are coupled,  $\kappa = 0$  corresponds to band crossing, whereas  $\kappa \neq 0$  corresponds to anticrossing. As shown in Fig. 8(b), when  $g = 0.5a$ , the two “ $\pm$ ” guided modes of the TE mode precisely result in  $\kappa = 0$ , leading to a band crossing phenomenon, while when  $g \neq 0.5a$ , from a perturbative perspective, it is equivalent to a slight perturbation in the dielectric constant  $\kappa \propto \int \vec{E}_{n_1}^k(\vec{r}) \cdot \vec{E}_{n_2}^{k*}(\vec{r}) [\epsilon(x, y, z) + \Delta\epsilon(x, y, z)] d^3\vec{r}$ , leading to the guided mode coupling coefficient  $\kappa \neq 0$ , thus resulting in the anticrossing phenomenon, with the degeneracy point being opened. Therefore, this is an accidental degeneracy caused by the coupling strength  $\kappa = 0$ , rather than determined by symmetry. This can be further rigorously analyzed through asymmetric space group theory [31,37].

#### APPENDIX D: EXPERIMENTAL FEASIBILITY AND TOPOLOGICAL PROPERTIES

The TRCs discussed can be achieved by employing all-dielectric materials on a silicon-based platform. This process can be facilitated through a complementary metal-oxide semiconductor compatible nanofabrication [16]. For example, electron-beam lithography can be utilized to manufacture two-dimensional photonic crystal slabs [38].

Additionally, a scanning near-field optical microscope system has been utilized to characterize the performance of a

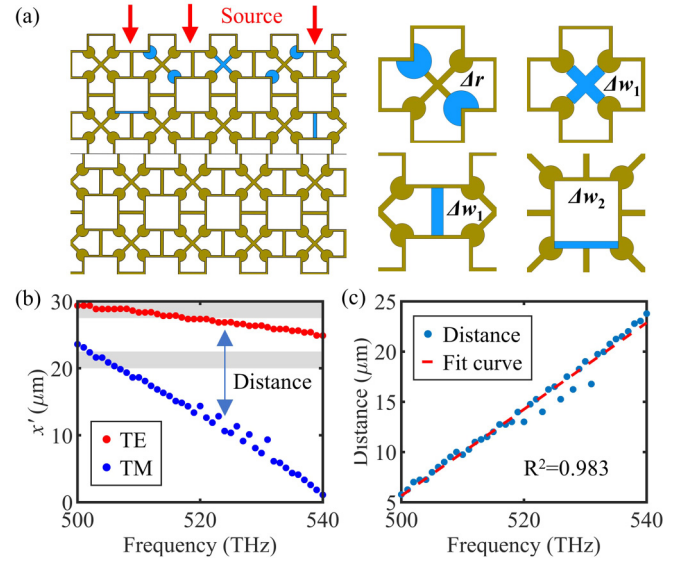


FIG. 9. (a) The schematic diagram illustrates the TRC with defects constructed via the inclined axis, where  $\Delta r$ ,  $\Delta w_1$ , and  $\Delta w_2$  are all set to 10%. (b) The frequency-dependent variation of peak intensity positions for TE and TM modes of the inclined axis TRC. The gray bands correspond to defect positions. (c) The variation of separation distances between TE and TM modes of the inclined axis TRC with frequency, featuring a red dashed line denoting the fitted curve.

TRC in Ref. [1]. This further demonstrates the feasibility and practicality of the proposed experimental setup.

Fabrication errors may result in machining deviations in the photonic crystal unit-cell structure. In Fig. 9(a), we investigate the localized impact of such TRCs on light under these circumstances. It is noteworthy that despite machining deviations, the localized positional changes are minor. Furthermore, we plotted the relationship between frequency and peak intensity positions, as well as the variation in separation distance between TE and TM modes with frequency [Figs. 9(b) and 9(c)]. We observed that both the peak intensity position and the separation distance still exhibit a linear relationship with frequency.

In the paper, we also introduced methods to increase  $nx$  and introduce  $\delta$  to optimize the determination of localized positions, which further enhances the accuracy of the judgment. In conclusion, our structure exhibits immunity to defects, providing a stable and reliable solution for spectral analysis and frequency division multiplexing.

- [1] C. Lu, Y.-Z. Sun, C. Wang, H. Zhang, W. Zhao, X. Hu, M. Xiao, W. Ding, Y.-C. Liu, and C. T. Chan, On-chip nanophotonic topological rainbow, *Nat. Commun.* **13**, 2586 (2022).
- [2] C. Lu, C. Wang, M. Xiao, Z. Q. Zhang, and C. T. Chan, Topological rainbow concentrator based on synthetic dimension, *Phys. Rev. Lett.* **126**, 113902 (2021).
- [3] Y. Ruan, X. Qian, H.-X. Wang, Z.-D. Hu, Y. Yang, J. Wang, X. Shen, and Y. Wang, Applications for wavelength division multiplexers based on topological photonic crystals, *Photon. Res.* **11**, 569 (2023).
- [4] G. Chaplain, D. Pajer, J. M. De Ponti, and R. Craster, Delineating rainbow reflection and trapping with applications for energy harvesting, *New J. Phys.* **22**, 063024 (2020).
- [5] K. L. Tsakmakidis, O. Hess, R. W. Boyd, and X. Zhang, Ultra-slow waves on the nanoscale, *Science* **358**, eaan5196 (2017).
- [6] K. L. Tsakmakidis, A. D. Boardman, and O. Hess, ‘Trapped rainbow’ storage of light in metamaterials, *Nature (London)* **450**, 397 (2007).
- [7] Q. Gan, Y. J. Ding, and F. J. Bartoli, “Rainbow” trapping and releasing at telecommunication wavelengths, *Phys. Rev. Lett.* **102**, 056801 (2009).



- [8] B. Davies, G. J. Chaplain, T. A. Starkey, and R. V. Craster, Graded quasiperiodic metamaterials perform fractal rainbow trapping, *Phys. Rev. Lett.* **131**, 177001 (2023).
- [9] Q. Gan, Z. Fu, Y. J. Ding, and F. J. Bartoli, Ultrawide-bandwidth slow-light system based on THz plasmonic graded metallic grating structures, *Phys. Rev. Lett.* **100**, 256803 (2008).
- [10] T. Baba, Slow light in photonic crystals, *Nat. Photon.* **2**, 465 (2008).
- [11] S. Elshahat, M. S. M. Esmail, H. Yuan, S. Feng, and C. Lu, Broadband multiple topological rainbows, *Ann. Phys. (NY)* **534**, 2200137 (2022).
- [12] H. Zhang, L. Qian, C. Wang, C.-Y. Ji, Y. Liu, J. Chen, and C. Lu, Topological rainbow based on graded topological photonic crystals, *Opt. Lett.* **46**, 1237 (2021).
- [13] J. Chen, W. Liang, and Z.-Y. Li, Switchable slow light rainbow trapping and releasing in strongly coupling topological photonic systems, *Photon. Res.* **7**, 1075 (2019).
- [14] L.-H. Wu and X. Hu, Scheme for achieving a topological photonic crystal by using dielectric material, *Phys. Rev. Lett.* **114**, 223901 (2015).
- [15] S. Barik, H. Miyake, W. DeGottardi, E. Waks, and M. Hafezi, Two-dimensionally confined topological edge states in photonic crystals, *New J. Phys.* **18**, 113013 (2016).
- [16] X.-T. He, E.-T. Liang, J.-J. Yuan, H.-Y. Qiu, X.-D. Chen, F.-L. Zhao, and J.-W. Dong, A silicon-on-insulator slab for topological valley transport, *Nat. Commun.* **10**, 872 (2019).
- [17] T. Ozawa, H. M. Price, A. Amo, N. Goldman, M. Hafezi, L. Lu, M. C. Rechtsman, D. Schuster, J. Simon, O. Zilberberg, and I. Carusotto, Topological photonics, *Rev. Mod. Phys.* **91**, 015006 (2019).
- [18] L. Lu, J. D. Joannopoulos, and M. Soljačić, Topological photonics, *Nat. Photon.* **8**, 821 (2014).
- [19] A. Psarouli, A. Salapatas, A. Botsialas, P. Petrou, I. Raptis, E. Makarona, G. Jobst, K. Tukkiemi, M. Sopanen, R. Stoffer *et al.*, Monolithically integrated broad-band Mach-Zehnder interferometers for highly sensitive label-free detection of biomolecules through dual polarization optics, *Sci. Rep.* **5**, 17600 (2015).
- [20] X. Yi, Y.-F. Xiao, Y. Li, Y.-C. Liu, B.-B. Li, Z.-P. Liu, and Q. Gong, Polarization-dependent detection of cylinder nanoparticles with mode splitting in a high-q whispering-gallery microresonator, *Appl. Phys. Lett.* **97**, 203705 (2010).
- [21] D. Dai, C. Li, S. Wang, H. Wu, Y. Shi, Z. Wu, S. Gao, T. Dai, H. Yu, and H.-K. Tsang, 10-channel mode (de) multiplexer with dual polarizations, *Laser Photonics Rev.* **12**, 1700109 (2018).
- [22] X.-T. He, C.-H. Guo, G.-J. Tang, M.-Y. Li, X.-D. Chen, and J.-W. Dong, Topological polarization beam splitter in dual-polarization all-dielectric valley photonic crystals, *Phys. Rev. Appl.* **18**, 044080 (2022).
- [23] Y. Chen, F. Meng, Z. Lan, B. Jia, and X. Huang, Dual-polarization second-order photonic topological insulators, *Phys. Rev. Appl.* **15**, 034053 (2021).
- [24] B. Shen, P. Wang, R. Polson, and R. Menon, An integrated-nanophotonics polarization beamsplitter with  $2.4 \times 2.4 \mu\text{m}^2$  footprint, *Nat. Photon.* **9**, 378 (2015).
- [25] J. A. Iglesias Martínez, N. Laforge, M. Kadic, and V. Laude, Topological waves guided by a glide-reflection symmetric crystal interface, *Phys. Rev. B* **106**, 064304 (2022).
- [26] F. Liu and K. Wakabayashi, Novel topological phase with a zero berry curvature, *Phys. Rev. Lett.* **118**, 076803 (2017).
- [27] F. Liu, H.-Y. Deng, and K. Wakabayashi, Topological photonic crystals with zero Berry curvature, *Phys. Rev. B* **97**, 035442 (2018).
- [28] Z. Zhang, M. Rosendo López, Y. Cheng, X. Liu, and J. Christensen, Non-Hermitian sonic second-order topological insulator, *Phys. Rev. Lett.* **122**, 195501 (2019).
- [29] Z.-M. Zhan, P.-Y. Guo, W. Li, H.-X. Wang, and J.-H. Jiang, Topological light guiding and trapping via shifted photonic crystal interfaces, *Appl. Phys. Lett.* **123**, 251107 (2023).
- [30] Y. Chen, H.-X. Wang, Z. Lan, and Z. Su, Dual-polarization helical interface states in inverse-designed photonic crystals with glide symmetry, *Phys. Rev. B* **109**, 075132 (2024).
- [31] A. Mock, L. Lu, and J. O'Brien, Space group theory and fourier space analysis of two-dimensional photonic crystal waveguides, *Phys. Rev. B* **81**, 155115 (2010).
- [32] N. Khan, P. Wang, Q. Fu, C. Shang, and F. Ye, Observation of period-doubling Bloch oscillations, *Phys. Rev. Lett.* **132**, 053801 (2024).
- [33] O. Khayam and H. Benisty, General recipe for flatbands in photonic crystal waveguides, *Opt. Express* **17**, 14634 (2009).
- [34] J. Zak, Berry's phase for energy bands in solids, *Phys. Rev. Lett.* **62**, 2747 (1989).
- [35] H.-X. Wang, G.-Y. Guo, and J.-H. Jiang, Band topology in classical waves: Wilson-loop approach to topological numbers and fragile topology, *New J. Phys.* **21**, 093029 (2019).
- [36] E. Lidorikis, M. M. Sigalas, E. N. Economou, and C. M. Soukoulis, Gap deformation and classical wave localization in disordered two-dimensional photonic-band-gap materials, *Phys. Rev. B* **61**, 13458 (2000).
- [37] A. P. Cracknell, Tables of the irreducible representations of the 17 two-dimensional space groups and their relevance to quantum mechanical eigenstates for surfaces and thin films, *Thin Solid Films* **21**, 107 (1974).
- [38] C. P. Reardon, I. H. Rey, K. Welna, L. O'Faolain, and T. F. Krauss, Fabrication and characterization of photonic crystal slow light waveguides and cavities, *J. Vis. Exp.* **69**, e50216 (2012).